**Gen Satoh**
Mechanical Engineering Department,
Columbia University,
New York, NY 10027

**Xu Huang**

**Ainissa G. Ramirez**

Mechanical Engineering Department,
Yale University,
New Haven, CT 06511

**Y. Lawrence Yao**
Mechanical Engineering Department,
Columbia University,
New York, NY 10027

# Characterization and Prediction of Texture in Laser Annealed NiTi Shape Memory Thin Films

*Thin film shape memory alloys are a promising material for use in microscale devices for actuation and sensing due to their strong actuating force, substantial displacements, and large surface to volume ratios. NiTi, in particular, has been of great interest due to its biocompatibility and corrosion resistance. Effort has been directed toward adjusting the microstructure of as-deposited films in order to modify their shape memory properties for specific applications. The anisotropy of the shape memory and superelastic effects suggests that inducing preferred orientations could allow for optimization of shape memory properties. Limited work, however, has been performed on adjusting the crystallographic texture of these films. In this study, thin film NiTi samples are processed using excimer laser crystallization and the effect on the overall preferred orientation is analyzed through the use of electron backscatter diffraction and X-ray diffraction. A three-dimensional Monte Carlo grain growth model is developed to characterize textures formed though surface energy induced abnormal grain growth during solidification. Furthermore, a scaling factor between Monte Carlo steps and real time is determined to aid in the prediction of texture changes during laser crystallization in the partial melting regime.* [DOI: 10.1115/1.4007459]

## Introduction

Originally considered for use in bulk form, shape memory alloys have garnered enhanced interest as materials for use in microelectromechanical (MEMS) devices due to their strong actuating force and large displacement capabilities [1]. Particular emphasis has been placed on the use of shape memory alloys in thin film form to create active and passive MEMS devices due to their reduced thermal mass, and thus decreased response time. The use of these materials, however, requires careful control over their composition, microstructure, and mechanical loading which can all significantly affect their shape memory responses.

Various methods have been proposed and investigated for adjusting or enhancing the properties of shape memory materials from furnace annealing to laser crystallization. These methods have shown the ability to adjust phase transformation temperatures as well as the level of available shape memory recovery through changes in matrix composition, stress, and microstructure. One shape memory material, near-equiatomic nickel titanium (NiTi), has been the focus of a large portion of these types of investigations. NiTi has been used as an actuator in applications ranging from microgrippers to microvalves and is of particular interest due to its strong shape memory response and biocompatibility [1,2].

Examples of recent work on NiTi include the use of furnace annealing to adjust the microstructure of bulk shape memory alloys (SMA) to control phase transformation temperatures by Ishida et al. [3] as well as the current authors [4] and the use of laser crystallization to control phase transformation temperatures through changes in film stress by Birnbaum et al. [5]. Furthermore, a significant effort has been put toward characterizing and modifying the microstructures of the materials as well as modeling of the shape memory response [6–8]. One aspect of these materials that has not yet been optimized, however, is their preferred orientation or crystallographic texture. Deformation of single crystal shape memory samples by Gall et al. [9] has shown that the shape memory response is anisotropic with certain orientations exhibiting superior shape memory properties. Texture in bulk shape memory materials caused by rolling processes has also been shown to produce anisotropic SMA sheets [10]. While both single crystals and rolled sheets have been shown to enable anisotropic SMA responses, these materials are not practical for use in MEMS devices. Thin films are easily deposited using equipment typically used in MEMS device fabrication and have the added advantage of enhanced actuation frequencies due to their larger surface to volume ratios. These observations suggest that the shape memory properties of thin film SMA could be further enhanced by tailoring the crystallographic texture to specific applications. Tailored microstructures could conceivably enhance film homogeneity or enable stronger, anisotropic shape memory responses for complex actuation applications.

The introduction of crystallographic texture into thin films has been achieved in various materials using many different processes. High-temperature deposition of films has been shown to produce strong fiber textures in NiTi and Cu films among others [7,11]. Another process for introducing textures in thin films is laser melt crystallization using excimer laser irradiation. It has been shown to enhance the fiber textures in Cu, Al, Si, and GaAs films [12–15] and through careful processing, the ability to impart in-plane textures in Cu [16]. While both methods have demonstrated the ability to induce textures, a significant advantage of laser crystallization compared with high-temperature deposition or furnace annealing is the spatial resolution that can be achieved, enabling selective processing, and thus texture variations within a single film.

In this study, the effects of excimer laser processing on the crystallographic texture of sputtered NiTi shape memory thin films are examined through the use of electron-backscatter diffraction and X-ray diffraction. Texture evolution is described using surface energy considerations in abnormal grain growth during film solidification. A three-dimensional Monte Carlo model is developed to help further understand the evolution of texture during laser melting and solidification.

## Background

**Texture Formation.** The use of a homogenized laser source and mask imaging to melt thin films allows for precise control over the induced melt depth and temperature profile. The small

Contributed by the Manufacturing Engineering of ASME for publication in the Journal of Manufacturing Science and Engineering. Manuscript received March 23, 2010; final manuscript received July 26, 2012; published online September 10, 2012. Assoc. Editor: Kornel Ehmann.

absorption depth of UV light in metals causes the overwhelming majority of the laser energy to be absorbed by the film rather than the substrate. At sufficient laser intensities, a portion or the entire thickness of the film can be melted. Due to limited heating of the substrate the primary mode of heat dissipation is conduction through the substrate and subsequent solidification occurs vertically from the remaining solid portions of the film or the substrate surface. In addition, due to the large processing area and homogenous energy distribution, heat flow can be considered to be nearly one-dimensional over most of the processed geometry.

One effect of this configuration is the stabilization of the liquid–solid interface to fluctuations. Solidification of a laser-melted film on a cool substrate can be represented by the thermal gradient being positive in the direction of growth. This causes the interface to become stable as protrusions in the interface encounter higher temperatures farther into the liquid and their growth slows. Growth of a solid into an undercooled liquid, on the other hand, can result in a dendritic or cellular growth structure due to destabilization of the interface. In NiTi, which undergoes a congruent transformation between liquid and solid, no solute partitioning is expected to occur during solidification and thus constitutional supercooling is not a factor in destabilizing the interface [17]. Thus, the solid–liquid interface during laser-induced rapid solidification of NiTi is expected to be planar in geometry. The textures generated by dendritic and planar growth will differ due to the varying mechanisms of growth. During dendritic solidification texture is created by the higher growth velocity of dendrites with preferred orientations. In cubic materials this generally results in a (100) normal texture.

During planar growth, normal grain growth is dictated by the reduction of grain boundary energy causing grains of all orientations to grow isotropically without changing the overall film texture. In many cases, however, growth does not occur isotropically; the driving force is no longer only grain boundary energy but includes effects from various other considerations such as strain energy and surface energy. Many of these effects are anisotropic which causes them to promote the growth of certain grain orientations more than others. This leads to anisotropies in the growth rate and nonuniform grain sizes. This type of growth is termed abnormal grain growth. Through this mechanism, the enhanced growth rate of certain preferred orientations can then lead to an overall preferred orientation in the sample.

**Laser Crystallization.** Crystallization and grain growth in thin films through melt-mediated laser processing can be separated into three regimes as described by Im et al. [18]. In the partial melting regime a portion of the film is melted such that a solid layer remains on the substrate and grain growth occurs from the remaining solid–liquid interface. This growth occurs close to the melting temperature of the material since there is no need for nucleation which generally requires significant undercooling. For initially crystalline materials this can result in epitaxial regrowth from the remaining grains, preserving their orientations. Strengthening of texture can occur in these films if anisotropies cause grains with preferred orientations to grow faster than others.

In the complete melting regime the entire thickness of the film is melted and thus crystallization of these films requires first nucleation and then growth. The nucleation can occur either homogeneously within the film or heterogeneously at the substrate-liquid interface. Heterogeneous nucleation on the substrate can induce a preferred orientation if interface energy effects lead to greater nucleation of seeds of a particular orientation. In the near-complete melting regime the majority of the film is melted while a small number of solid seeds remain on the substrate. Texture generation in this regime is caused by the anisotropy in the growth velocity of the remaining seeds as well as any preferred orientation within the nucleated grains. Experiments performed within this study are limited primarily to processing within the partial melting regime and thus textures are thought to form through anisotropies during epitaxial growth from the remaining solid layer.

## Experimental Setup

One micrometer thick Ni-rich NiTi samples were deposited on silicon substrates over a 1 $\mu$m ultra-low residual stress $Si_3N_4$ barrier layer. This barrier layer is used to limit the formation of silicides at the film-substrate interface. The films were deposited through magnetron sputter deposition of a NiTi alloy target and a pure Ti target whose powers were tuned to achieve the desired composition. Further details on film deposition are described in Lee and Ramirez [19]. The final composition of the films was 49.6 at. % Ti-Ni as determined through energy dispersive X-ray spectroscopy. The deposition was performed at the room temperature which results in an amorphous structure and films were annealed in a vacuum tube furnace at 460 °C for 5 min in order to crystallize them prior to laser irradiation.

Laser crystallization of the samples was performed using a XeCl excimer laser at a wavelength of 308 nm. A projection mask system was used to selectively irradiate areas of the film with 320 $\mu$m or 1.2 mm square spots. The beam was homogenized in order to maintain uniform energy density within each processed region. Laser processing was performed at various energy densities between 533 and 1333 mJ/cm$^2$ at ambient temperature in air. Large area processing for X-ray diffraction analysis was also performed by translation of the sample under the laser beam creating an array of single pulse irradiated regions. In situ transient reflectance measurements were performed on the samples during irradiation to determine the melt-duration using a HeNe laser probe.

Following laser crystallization samples were characterized using X-ray diffraction (XRD) in order to determine the phases and texture of the films. Use of Ni-rich films typically results in transformation temperatures below room temperature. All films were confirmed to be austenitic at room temperature which allows for all XRD measurements to be performed at room temperature for texture analysis. Electron backscatter diffraction (EBSD) measurements of films were also performed on annealed and laser processed samples. Samples were etched using a mixture of 2 ml HF, 6 ml $HNO_3$, and 92 ml $H_2O$ (Kroll's reagent) applied with a cotton swab for 15 s prior to EBSD measurements to remove the oxide layer from the top surface. EBSD measurements were performed at an accelerating voltage of 25 kV and a working distance of 10 mm at resolutions of 0.25 to 1 $\mu$m. Differential interference contrast (DIC) optical micrographs of samples were also taken in order to confirm the grain sizes observed through EBSD.

## Numerical Simulation

In order to model grain growth within the film during solidification in the partial melting regime a three-dimensional Monte Carlo grain growth model has been developed. While Monte Carlo models have been used to determine solid phase grain growth during annealing processes for some time, more recently, they have been used to model abnormal grain growth as well as the deposition processes [20,21]. These advancements require reworking the traditional Monte Carlo process as well as the consideration of energy anisotropies between grains. A brief overview of the Monte Carlo process is included below while emphasis has been placed on the extension to three-dimensional growth developed by the authors.

**Single Layer Monte Carlo.** Similar to most two-dimensional Monte Carlo models, this model is structured around a mesh with each node representing a small area of material. The mesh is a $500 \times 500$ element array with each node representing a 1.33 $\mu$m square area. The orientation of each node is represented by an integer number between 1 and 24 and contiguous areas with the same orientation represent grains. A schematic representation of a

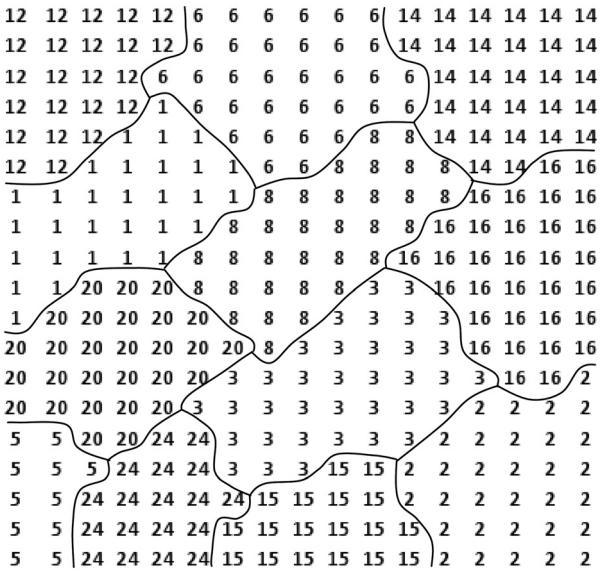


**Fig. 1 Schematic representation of grains within two-dimensional Monte Carlo model. Orientation of each node is represented by an integer number between 1 and 24. Each node represents a 1.33 $\mu$m square area. Connected nodes with identical orientations represent grains. Grain boundaries (solid lines) separate nodes with different orientations and are added for clarity.**

typical two-dimensional Monte Carlo model is shown in Fig. 1. Within the Monte Carlo model the energy of a node at site $i$ is defined as

$$G_i = e_{gb} \sum_{n.n} (\delta_{s_i s_j} - 1) + e_{s_i} \tag{1}$$

where $e_{gb}$ is the grain boundary energy, $e_{si}$ is the surface energy, and $\delta_{sisj}$ is the Kronecker delta function. For each neighbor that is a different orientation than the current node, one unit of grain boundary energy is added. A surface energy component, $e_{si}$, is also added to the total node energy. Since surface energy values for NiTi were unavailable, typical values for a base-centered cubic (BCC) structured metal were obtained from Zhang et al. [22] for 24 separate orientations. The values used in the model are shown in Fig. 2 and significant orientation dependence can be observed with a minimum occurring for the (110) orientation.

Grain growth is modeled by attempting to reorient randomly chosen nodes such that their overall energy is decreased. Each Monte Carlo step (MCS) represents a series of reorientation attempts equal to the total number of nodes in the mesh. During each reorientation attempt the initial and trial node energies are calculated by entering the current orientation and a randomly selected trial orientation respectively into Eq. (1). The probability of each reorientation occurring is then determined using the metropolis transition function

$$p = \begin{cases} e^{\left(-\frac{\Delta G}{k_b T}\right)} & \text{if} \quad \Delta G > 0 \\ 1 & \text{if} \quad \Delta G < 0 \end{cases} \tag{2}$$

where $\Delta G$ represents the change in energy caused by the change in orientation and $T$ is the temperature of the solid surface. The inclusion of anisotropic surface energy in the overall node energy causes specific orientations to have, on average, lower energies. As a result, the probability of switching to those orientations is greater which causes surface energy induced abnormal grain growth to occur.

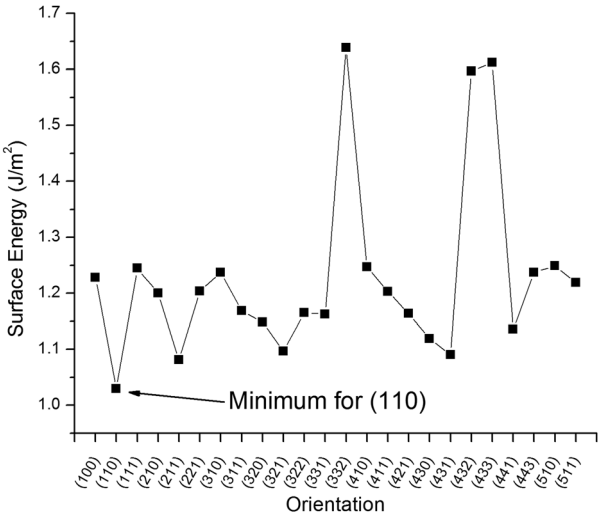


**Fig. 2 Surface energies for various orientations for typical base-centered cubic metal. Note significant anisotropy and minimum surface energy for (110) normal orientation.**

**Three-Dimensional Growth.** Unlike solid-phase grain growth models where the amount of solid material is constant, during solidification new material is continually being added to the solid surface. Thus, in order to model grain growth due to solidification a multilayer Monte Carlo method is adopted. This method employs multiple two-dimensional Monte Carlo models run consecutively, each representing a layer of new material that has solidified onto the existing surface and is similar in principle to models developed by Srolovitz [21] and Jung et al. [23]. Within each layer the model is run in the traditional fashion as described above for one MCS. The initial orientation of each node of the new layer is considered to be the same as in the preceding layer.

In order to determine the thickness of each layer the scaling factor between Monte Carlo steps and melt depth must be determined. Using first-order interface kinetics, the flux of atoms arriving on the solid interface from the liquid phase is described by [24]

$$I_{l\to s} = n_a^l \nu e^{\left(-\frac{G_A}{k_b T}\right)} \tag{3}$$

where $n_a^l$ is the number of atoms per unit area in the liquid phase, $\nu$ is the jump frequency, $G_A$ is the activation energy required to perform the jump, $k_b$ is the Boltzmann constant, and $T$ is the temperature. The flux in the reverse direction, from the solid to the liquid is written as

$$I_{s\to l} = n_a^s \nu e^{\left(-\frac{G_A + \Delta G_{\text{atom}}}{k_b T}\right)} \tag{4}$$

where $n_a^s$ is the number of atoms per unit area in the solid phase and $\Delta G_{\text{atom}}$ is the change in free energy due to the movement of one atom from the solid to the liquid. The net flux between the solid and liquid phases is the difference between Eqs. (3) and (4). For simplicity we assume that $n_a^l$ and $n_a^s$ are equal. The net flux is then multiplied by the atomic volume, $\Omega$, which results in an interface velocity

$$V = \Omega I_{\text{net}} = \Omega n_a \nu e^{\left(-\frac{G_a}{k_b T}\right)} \left[1 - e^{\left(-\frac{\Delta G_{\text{atom}}}{k_b T}\right)}\right] \tag{5}$$

Within each Monte Carlo step, each 1.33 $\mu$m long element must be consumed by grain growth. Since each layer of the model is two-dimensional, the velocity from Eq. (5) is considered to be the velocity at which solidified islands grow within the plane of the

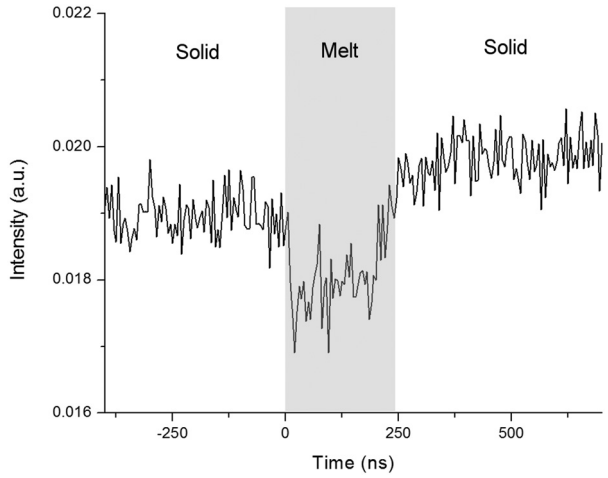


**Fig. 3 Transient reflectance measurement during laser processing of a single 320 $\mu$m square area near the complete melt threshold. Reflected signal from 632 nm HeNe laser source. Note melt duration of about 250 ns.**

film. Using this velocity the time required to complete each Monte Carlo step can be calculated. The experimentally determined melt duration can then be used to determine the required number of Monte Carlo steps to achieve solidification of a similar thickness. A similar methodology is described by Raabe [25] using grain boundary mobility to determine the scaling factor. Figure 3 shows typical transient reflectance data obtained during melting of a 1 $\mu$m thick NiTi film. The total melt duration is on the order of 250 ns and includes both melting and solidification. Using a simple two-dimensional finite element Fourier heat flow analysis (not shown) solidification is seen to start 100 ns after the pulse thus a solidification time of 150 ns is used to represent solidification of 1 $\mu$m of material.

The initial grains for the model are grown using an isotropic Monte Carlo grain growth model which is nearly identical to the anisotropic model except that it does not include considerations for surface energy. Orientations are randomly assigned to each node in the mesh and the isotropic Monte Carlo model is then run until the desired initial grain size is achieved. A flow-chart for both Monte Carlo models is shown in Fig. 4.

## Results and Discussion

In order to determine the initial grain size of the material, the as-annealed samples were etched using Kroll's reagent and observed under both optical microscopy and EBSD. Figure 5 is an optical micrograph showing the etched film surface. A distribution of grain sizes can be seen with the larger grains being on the order of 10 $\mu$m in diameter. An EBSD grain map is shown for comparison in Fig. 6 where grain boundaries are defined as locations where the misorientation angle between adjacent measurements is greater than 10 deg. The observed grain size and structure are very similar to those observed optically and which suggests that the chosen misorientation angle is appropriate. While both measurements show nearly equiaxed grains, it should be noted that they only characterize the surface of the films. The actual film thickness is only 1 $\mu$m, significantly smaller than the observed grain diameters, and thus the grains are much larger in the in-plane directions than they are in the normal direction. This type of grain shape is common and has been reported for many solid phase crystallized NiTi films [26].

Figure 7 shows the XRD spectra from the as-annealed sample as well as one for the as-deposited amorphous film. Five main peaks are observed in the crystallized sample, all of which can be indexed to austenitic NiTi. The largest peak, at $2\theta = 42.8$ deg is from the (110) orientation, while the other peaks at $2\theta = 61.9$ deg, 78.1 deg, 93.3 deg, and 108.7 deg are from the (200), (211), (220),

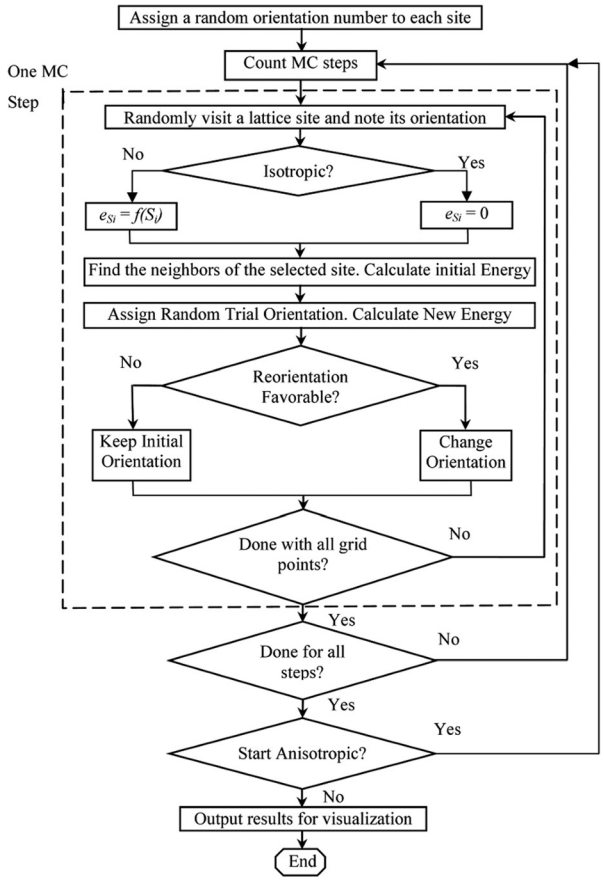


**Fig. 4 Flow chart for MC Model. Both isotropic and anisotropic models depicted. Isotropic model run first to set up initial grains for anisotropic model. Isotropic model neglects surface energy. Anisotropic model sets surface energy to be a function of orientation as shown in Fig. 2.**

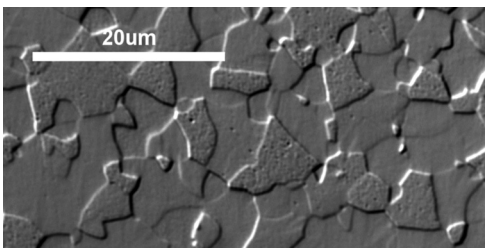


**Fig. 5 DIC Optical Image of furnace-annealed sample etched using Kroll's reagent. Note maximum grain size on the order of 10 $\mu$m. Clear delineation between adjacent grains. Distribution of grain sizes is also observed.**

and (310) orientations, respectively. The intensities of these peaks are observed to be in slightly different ratios than those from powder diffraction measurements which suggest that there may be a slight texture in the as-annealed samples. The as-deposited amorphous film shows a typical amorphous spectrum with a single broad peak. Since grains in annealed, amorphous NiTi are known to span the entire thickness of the film and within this study laser-crystallization experiments are performed almost exclusively under the partial melting regime, the observed grain size and texture are considered to be representative of the remaining solid layer irrespective of the melt depth.

**Surface Texture Characterization.** Figure 8(*a*) shows a representative EBSD map of a processed film with Euler angle

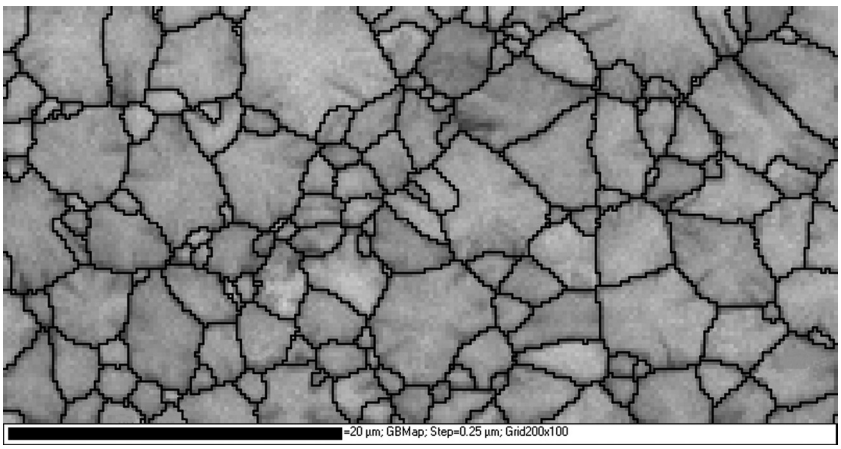


**Fig. 6 EBSD grain map of furnace annealed sample. Grain boundaries (solid lines) are shown where adjacent measurements have a misorientation angle of 10 deg or more. Grain shapes and sizes comparable to those observed through optical microscopy.**

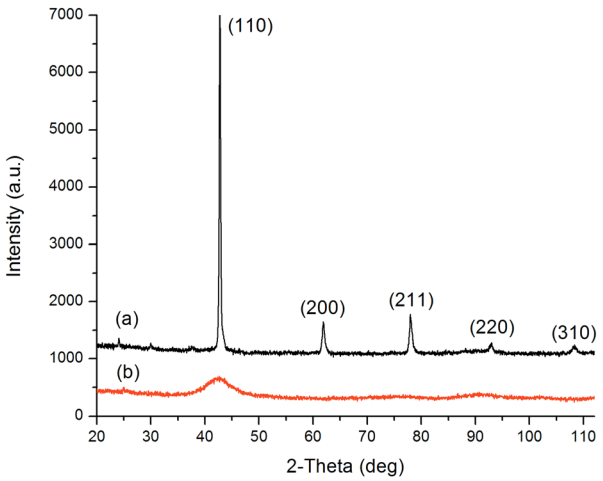


**Fig. 7 XRD spectra for (*a*) as-annealed and (*b*) as-deposited film obtained at room temperature. Note amorphous structure for as-deposited film and austenitic peaks for annealed sample.**

coloring covering an area of 100 $\mu$m by 50 $\mu$m. As above, grain boundaries are added at positions where adjacent measurements have greater than a 10 deg misorientation angle. The grain boundaries identified during post processing of the EBSD data can be seen to accurately separate areas with different orientations while maintaining a grain size distribution similar to that observed optically. Some isolated points do show orientations that are significantly different from their surroundings and are considered to be caused by surface defects or contamination within the film and to have little effect on the observed texture. Figure 8(*b*) is an inverse pole figure for the surface normal orientation which shows evidence of a (110) preferred orientation in the sample. As shown in Fig. 2, the (110) orientation has the lowest surface energy in BCC materials which can causes preferential growth of (110) oriented grains as the film solidifies and results in an increase in the area fraction of those grains. It should be noted that, since EBSD measurements are only affected by a thin surface layer of the film, unlike the solid phase crystallized films the observed texture is considered to be representative of only the top surface of the film and not the underlying volume. It will be shown, however, that an overall (110) normal texture is created in the samples through XRD measurements.

Figure 9 shows the same sample with grains of specific orientations highlighted, (100) for (a) and (110) for (b). Qualitatively it can be seen that (110) oriented grains are on average larger and more prevalent than those near the (100) orientation. It should be noted here that the multiplicity factor, the number of equivalent crystal planes in the lattice, for the (100) orientation is half that of the (110) orientation thus the highlighted grain area will be skewed toward the (110) even in randomly oriented samples. The observed differences, however, do suggest some preferential

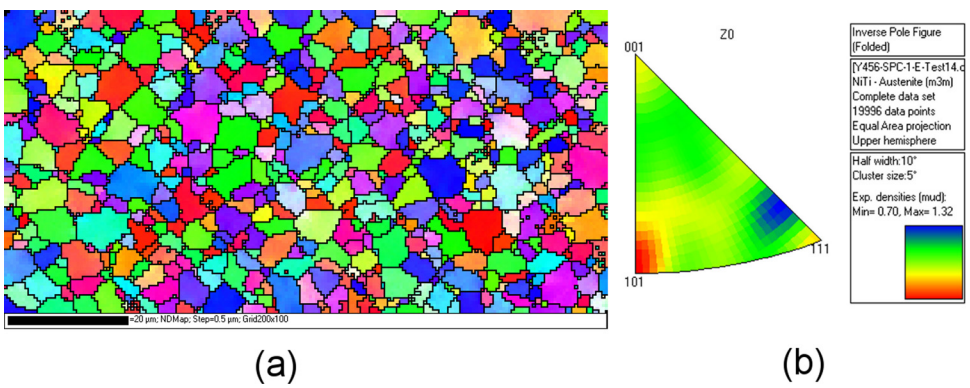


**Fig. 8 (*a*) EBSD map for normal direction of film processed at 909 mJ/cm$^2$ with Euler angle coloring. Grain boundaries (solid lines) are shown where adjacent measurements have a misorientation angle of 10 deg or more. Inverse pole figure (*b*) showing slight (110) texture normal to the film surface.**

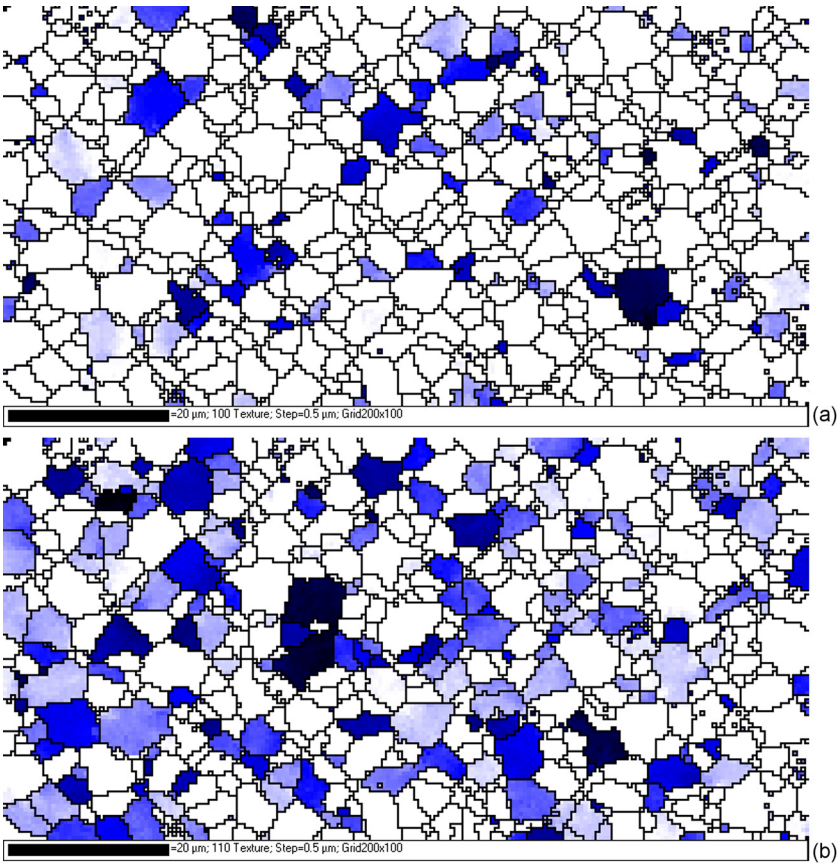


**Fig. 9 EBSD maps of sample processed at 909 mJ/cm$^2$ with different surface normal grain orientations highlighted. (*a*) (100) and (*b*) (110). Note overall larger grain size and greater density of (110) oriented grains. Multiplicity factor of (110) is twice that of (100) for BCC cubic materials.**

growth of (110) oriented grains which will be quantified using X-ray diffraction. Sections of an orientation distribution function (ODF) are shown in Fig. 10 with each pane having a constant value of $\phi_2$ where $\phi_1$, $\Phi$, and $\phi_2$ are Euler angles in the Bunge convention. The highest peaks in the ODF are at $\Phi = 45$ deg for $\phi_2 = 0$, 90 deg and near $\Phi = 90$ deg for $\phi_2$ near 45 deg. No significant dependence on $\phi_1$ is observed. Both of these orientations signify (110) normal orientations in cubic materials. The lack of dependence on $\phi_1$ indicates that the grains are randomly oriented in the in-plane directions. This is consistent with the solidification mechanism being vertical epitaxial regrowth from randomly oriented grains. The change in texture should only be in the surface normal direction due to abnormal in-plane grain growth.

As described above, in the Monte Carlo model the number of Monte Carlo steps performed is proportional to the melt depth. By using an activation energy, $G_A$, for Nickel of $9.15 \times 10^{-20}$ J/mol [27] and the heat of fusion of NiTi as 31.6 kJ/mol [28], the number of Monte Carlo steps required to model solidification of a 1 $\mu$m film was determined to be nine. For partially melted films grain growth occurs from the surface of the remaining solid material. Since solid phase crystallization of amorphous NiTi films has been shown to produce randomly oriented grains that span the thickness of the film [26], the initial grain size in the model is considered to be independent of melt depth and the grain orientations random. Different melt depths can be modeled by varying the number of Monte Carlo steps included in the model. Nickel was chosen to represent NiTi for the activation energy since it shares the same BCC structure. Figure 11 is a surface grain map derived from the Monte Carlo model after nine Monte Carlo steps where each color represents a different normal orientation. In-plane grain shapes are generally equiaxed and both small and large grains are observed. Overall, the morphology and size of the grains is similar to what is observed experimentally in Figs. 5 and 6 with the larger grains being roughly 10 $\mu$m and the smaller grains being 1 or 2 $\mu$m in diameter. Figure 12 shows grain maps of selected orientations, (110) and (200), after the initial and final Monte Carlo steps of the anisotropic model. As a whole, (110) oriented grains can be seen to grow in size during the course of the model. (200) oriented grains generally decrease in size with some disappearing completely by the final Monte Carlo step. This is due to the anisotropic growth rates captured by the model during solidification of the film. As seen in Fig. 2, the (110) orientation has one of the lowest surface energies of all the orientations included in the model while the (200) orientation has a much higher surface energy. Thus, during growth, the probability that an element will solidify with a (110) orientation is larger than the probability it will solidify with a (200) orientation. The complete disappearance of some grains is caused by occlusion by other, faster growing grains, likely with more preferred orientations. It should be noted; however, that each Monte Carlo step represents only a layer of material within the solid and thus, while grains may disappear from the surface as the number of steps increases, the grains are not completely removed from the material. It is also noted that no evidence of nucleation is observed in the model. As shown in Eq. (2), there is a possibility that a reorientation can occur even if it does not produce a net decrease in free energy. The probability of this occurrence, however, is nearly zero for even small increases in energy.

**Through-Thickness Texture Characterization.** Compared to EBSD measurements, XRD measurements are considered to better represent the texture of the films as they pertain to shape

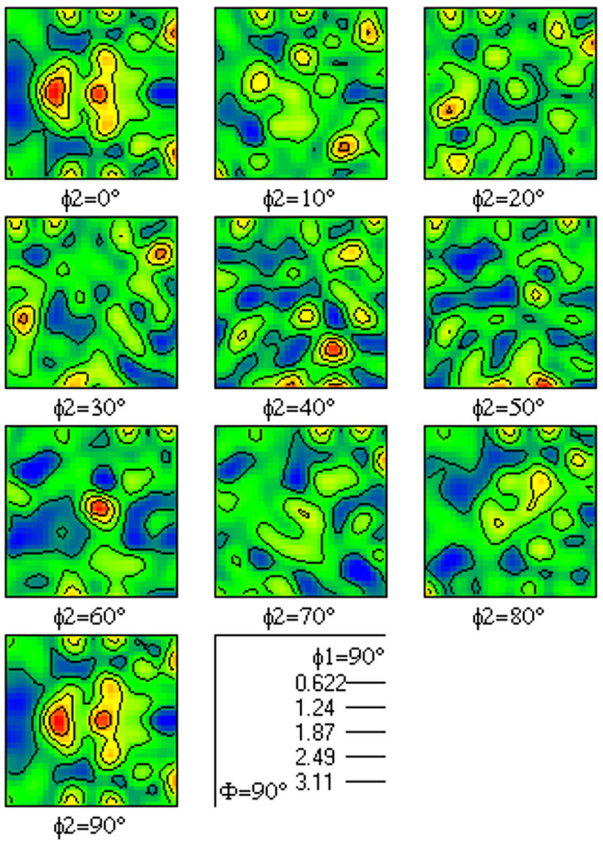


**Fig. 10 ODF for processed film showing peaks at $\Phi = 45$ deg for $\phi_2 = 0$, 90 deg and $\Phi = 90$ deg for $\phi_2$ near 45 deg suggesting (110) preferred orientation. Note lack of dependence on $\phi_1$ indicating random in-plane orientation. $\phi_1$, $\Phi$, and $\phi_2$ are Euler angles defined in the Bunge convention.**

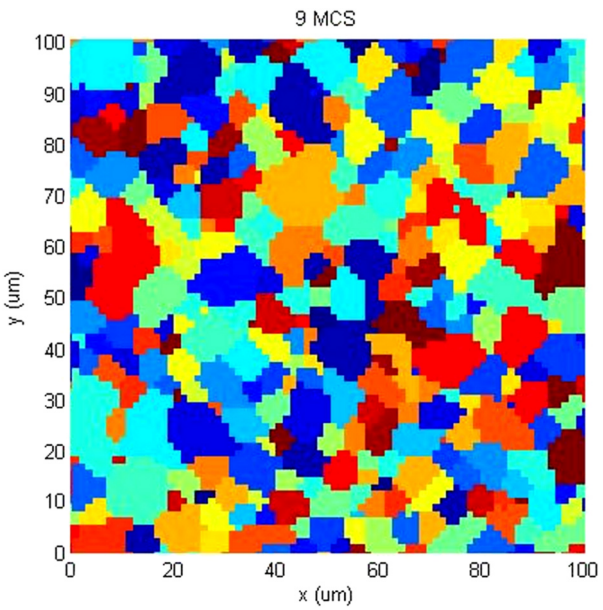


**Fig. 11 Surface grain map derived from anisotropic Monte Carlo simulation after nine Monte Carlo steps. Colors denote different surface normal orientations. Note grain shape and size distribution comparable to those observed experimentally through EBSD (Figs. 6 and 8(*a*)).**

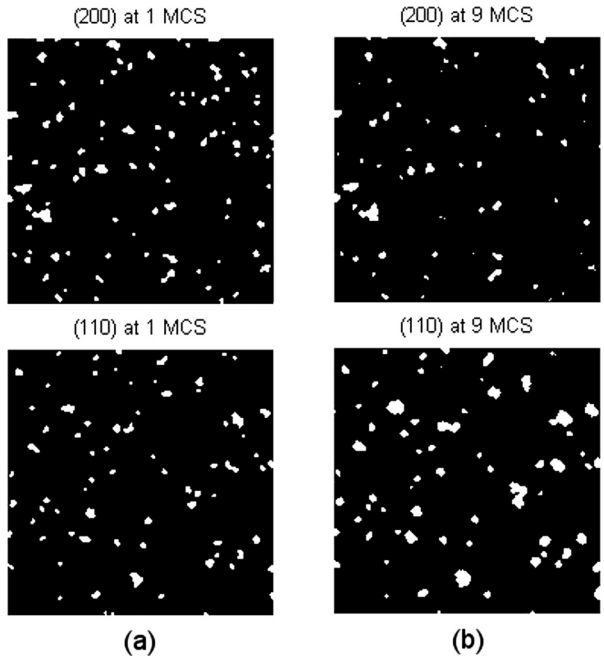


**Fig. 12 (110) and (200) oriented grains at (*a*) first MCS and (*b*) final MCS of the anisotropic Monte Carlo model. Growth of grains is observed for grains with low surface energy orientation (110). Grains with higher surface energy (200) decrease in size or disappear as number of MCS increases due to occlusion.**

memory applications since they measure the entire thickness of the film rather than just the surface layer. Deformation of thin film shape memory devices will generally not be limited to the surface of the film and thus characterization of the entire film thickness is critical to understanding the resulting mechanical response. Normalized XRD spectra for samples irradiated at different incident laser fluences are shown in Fig. 13. The three largest austenitic peaks, at $2\theta = 42.8$ deg, 61.9 deg, and 78.1 deg, are chosen to represent the texture in each sample since the smaller peaks are typically small and cannot be accurately characterized for all processing parameters. For laser processed samples, overall diffraction intensities were found to decrease with increasing energy

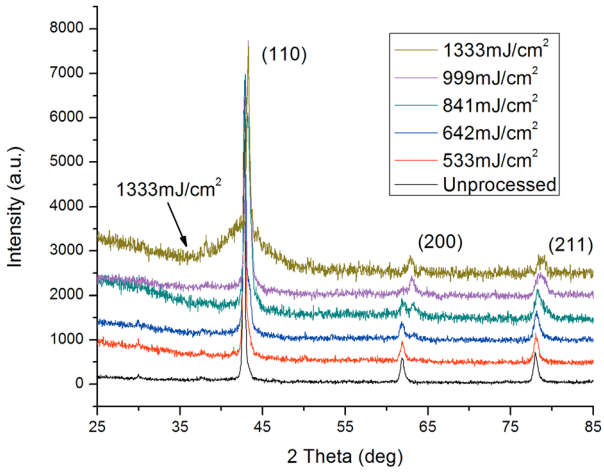


**Fig. 13 Normalized X-ray diffraction spectra for samples processed at various energy densities. Spectra shifted up in order of increasing energy density. Note shift in peaks toward higher $2\theta$ angles with increasing energy density as well as the peak broadening. Some amorphization of the material is considered to be occurring for highest energy density sample.**

density while no significant new diffraction peaks were observed. This suggests that the overall diffracting volume may be decreasing or that an amorphous layer may be forming on the film. A decrease in the diffracting volume may be caused by defective growth due to the extremely high growth velocities experienced during solidification. At very high growth rates the lack of sufficient time for diffusion has been shown to cause the structure to be a metastable crystalline or even amorphous phase [6]. In addition, it is possible that a Ti oxide layer is forming on the top of the sample as observed in nearly all thermally treated NiTi samples [29]. Some Ti-oxides are amorphous and would not be seen in the XRD spectra. The lack of new peaks in the XRD spectra after processing suggests that the formation of new crystalline phases during solidification is limited.

In addition to the changes in peak intensities observed in the XRD spectra, peak shifts toward higher $2\theta$ angles can be seen for all three diffraction peaks as energy densities increase. This signifies a decrease in d-spacing normal to the film surface caused by a likely increase in the in-plane tensile stress within the film. This effect is thought to be due to the contraction of the film during solidification against the stiff underlying substrate which experiences very little temperature change. It has been observed that stresses within materials may cause abnormal grain growth in grains under a biaxial stress state due to anisotropic strain energy densities [30]. This is driven by the anisotropies in the biaxial modulus of the material. For NiTi, strain energy densities are minimized for grains with (100) normal texture and maximized for grains with (111) normal texture and thus a (100) texture would be predicted if strain energy were to have a significant effect on grain growth.

XRD intensity calculations were also performed using data derived from the Monte Carlo grain growth model. Figure 14 shows the change in volume fraction of selected orientations with each Monte Carlo step within the anisotropic model. A significant divergence of the volume fractions of different orientations can be seen; caused by growth using anisotropic surface energy effects. When considered in the context of Fig. 2, the preferable low energy orientations are seen to increase in volume fraction while the higher energy orientations are seen to decrease in volume fraction. Figure 15 shows the evolution of the XRD spectra calculated using the volume fractions from the Monte Carlo model. The XRD intensities for the three main diffraction peaks of the furnace annealed sample are used as the nominal intensities and are then weighted by the calculated volume fractions to determine the new intensities. The XRD intensities are seen to change in accordance with the surface energy anisotropy accounted for in the model. As

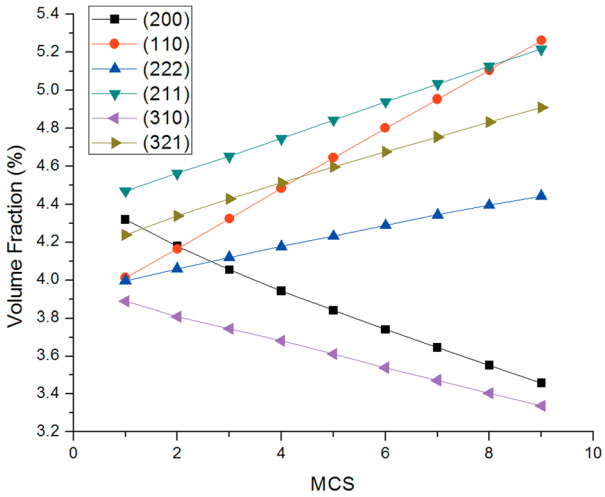


**Fig. 14 Volume fraction of grains with selected orientations from Monte Carlo simulation as a function of MCS. Note increase in volume fraction of low surface energy orientation (110) and decrease in volume fraction for high surface energy orientation (200).**

the number of steps increases, the film encounters more vertical growth and abnormal grain growth is able to enlarge grains with preferred orientations to a greater extent. In particular, the (110) peak shows a significant increase in intensity, while the (200) peak shows some decline and the (211) peak remains fairly constant as the number of Monte Carlo steps increases.

Figure 16 shows the fraction of the total X-ray diffraction intensity contributed by each of the three chosen orientations for both the experimental and numerical results. The error bars in the experimental results signify the standard deviation from four separate measurements. The intensity fraction from the (110) oriented grains increases monotonically while the intensity fractions for the (200) and (211) orientations decrease with both energy density and Monte Carlo steps. As described above, energy density and MCS are related through considerations of melt depth. For the current model, nine MCS or an energy density of 1333 mJ/cm$^2$ corresponds to a 1 $\mu$m melt depth. The numerical XRD results can be seen to accurately predict the change in intensity fractions for the three chosen diffraction peaks with changes in energy density.

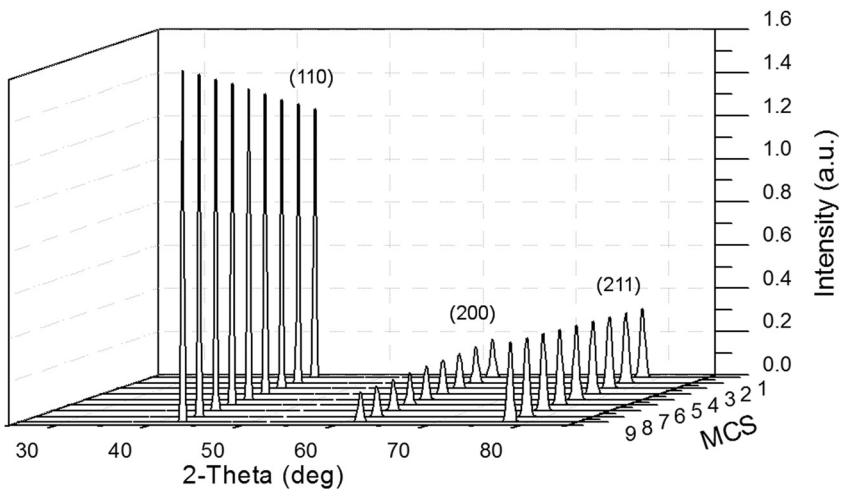


**Fig. 15 XRD spectra derived from Monte Carlo model volume fraction data for each MCS. Good agreement with experimentally determined normalized spectra (Fig. 13). Note increase in intensity of (110) peak at 42.8 deg, decrease in intensity of (200) peak at 61.9 deg, and near-constant intensity for (211) peak at 78.1 deg $2\theta$ with number of MCS.**

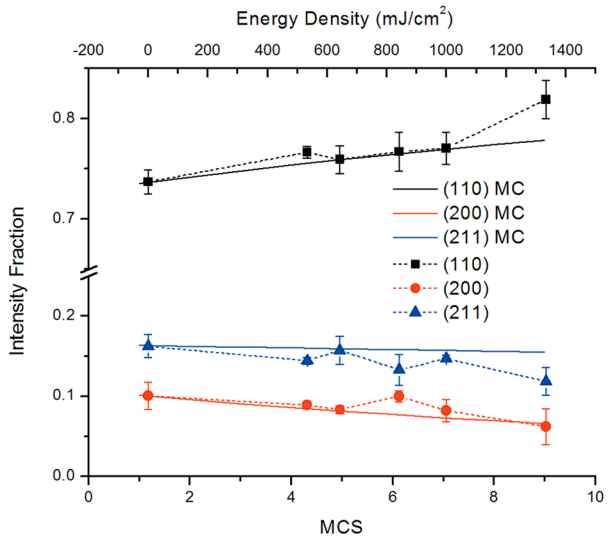


**Fig. 16 Intensity fraction versus MCS and energy density for MC and experimental measurements respectively. Good agreement between model and experimental values for all but highest energy density sample. Highest energy density sample is considered to be in the near-complete melting regime. Error bars denote standard deviation from four separate measurements.**

As described above, surface energy anisotropies in BCC samples promote (110) textures while strain energy anisotropies promote (200) textures during grain growth. Thus, the observed trends are consistent with secondary grain growth in laser processed samples being dominated by surface energy rather than strain energy effects.

While the agreement between the model and experimental results is strong for nearly all energy densities, experimental results at the highest energy density, 1333 mJ/cm$^2$, shows a stronger (110) texture than predicted by the model. This effect is believed to be caused by the film reaching the near-complete melting regime resulting in significant but not complete amorphization of the film. A wide peak in the same $2\theta$ range as the amorphous peak in Fig. 7 is observed in Fig. 13 for the film processed at 1333 mJ/cm$^2$ along with a sharp diffraction peak at 42.8 deg from the (110) orientation. It is considered that the fully melted areas of the film may be forming an amorphous structure rather than the equilibrium austenitic NiTi phase due to the exceedingly fast quench rate of the material. This would explain both the significantly increased peak width as well as the decrease in overall diffraction intensity from the film. The increased (110) texture observed in the film may be due to the enhanced growth rate of seeds with (110) orientation due to surface energy effects.

**Further Analysis.** Figure 17 shows a cross section view of the growing grains within the film as described by the Monte Carlo model and consists of nine Monte Carlo steps stacked upon each other. In-plane growth of grains can be seen resulting a v-shaped grain structure with some grains growing larger and some getting smaller as the film grows. This type of structure is characteristic of abnormal grain growth during solidification. Grains which get larger as solidification progresses have preferred orientations with low surface energies. Shrinking and occluded grains represent those grains that are not preferred due to their high surface energies. The growth of preferred orientations and the reduction and possible disappearance of others is consistent with the proposed mechanism of texture formation and was observed in Fig. 12 as well.

Figure 18 shows the percentage change in average grain size as a function of energy density for experimental results and as a function of Monte Carlo steps for numerical results. The average grain size for the sample processed with the highest energy density (1333 mJ/cm$^2$) could not be determined due to partial amorphization of the film. The overall growth rates observed experimentally and through the model show reasonable agreement both in direction and magnitude with overall average grain sizes increasing with greater vertical growth due to occlusion of smaller, less preferred grains. As described above, for EBSD or optical measurements of grain size, occluded grains are no longer visible and do not contribute to the calculated grain size. Overall, the numerical model underestimates the average grain size when compared to the experimental results. A possible explanation is that the actual surface energy anisotropy for NiTi is stronger than the typical BCC values used in the model. This would cause the lateral growth rate anisotropy to be underestimated by the model resulting in weaker abnormal grain growth.

The boundary between the processed and unprocessed regions of the surface of a film as observed through DIC optical microscopy is shown in Fig. 19(*a*). The unprocessed film surface is smooth with shallow and symmetric grain boundaries. The processed region, however, has a much rougher surface with significant surface relief observed between grains. This morphology suggests that certain grains grew at a faster rate during solidification from the solid–liquid interface or that the initial laser-induce melt depth was nonuniform and grain dependent. A cross section profile obtained through atomic force microscopy is shown in Fig. 19(*b*) and confirms the significant change in roughness in the processed region of the film. Grain boundaries in the unprocessed region of the film cannot be seen in the height profile; however, grain boundaries in the processed region are clearly visible and are on the order of 10 nm in height. This represents a high energy grain boundary configuration that would not be expected to occur at equilibrium. It is possible that the enhanced growth rate of certain grains relative to their neighbors due to surface energy anisotropies could lead to greater growth in the vertical direction. Due

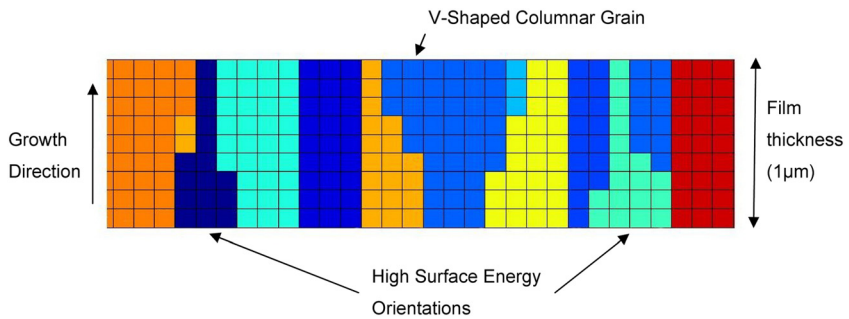


**Fig. 17 Sample cross section from Monte Carlo model for nine MC steps. Each color represents a different surface normal orientation while each cell represents a 1.33 $\mu$m wide element from the MC mesh. Continuous areas with the same color represent grains. Note v-shaped columnar grain structure indicative of abnormal grain growth. Not show to scale.**

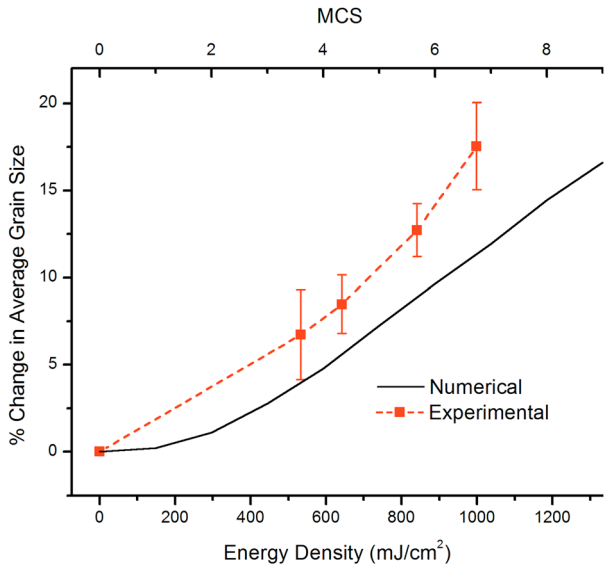


**Fig. 18 Percentage change in average surface grain size as a function of MCS and energy density for numerical and experimental results, respectively, showing increasing trend due to growth of preferentially oriented grains and occlusion of others. Grain size for highest energy density (1333 mJ/cm$^2$) not observed due to significant amorphization of film.**

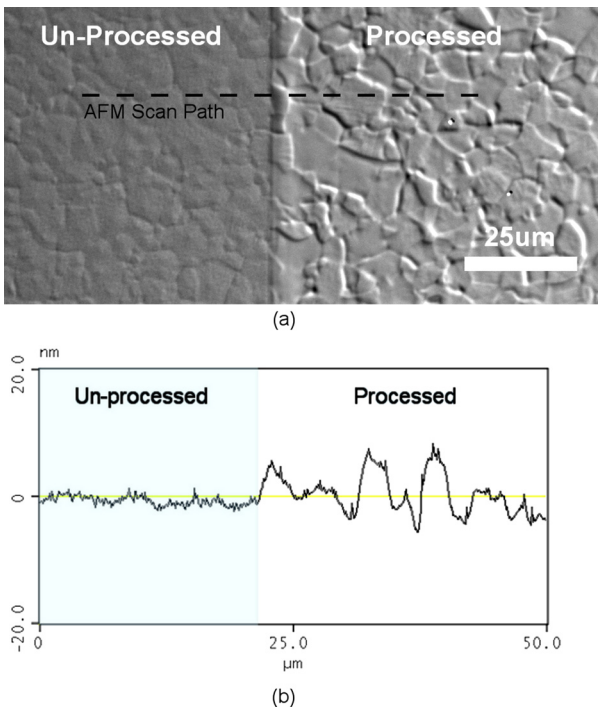


**Fig. 19 (*a*) Optical micrograph of boundary between processed and unprocessed regions. Note significant roughening of processed regions due to step grain boundaries. (*b*) AFM cross section shows significant change in surface roughness in processed region with adjacent grains having ~10 nm height difference.**

to the high solidification rate of the film the grain boundaries may not have enough time to reconfigure themselves to their preferred, symmetric low-energy configuration. Nonetheless, the increased surface roughness does suggest a significant deviation from equilibrium during the solidification of the laser-processed regions. It should be noted that the Monte Carlo model developed in this work assumes a uniform vertical growth rate and thus does not predict roughening of the film surface after solidification.

## Conclusion

In conclusion, it has been shown that the normal texture in crystalline Ni-rich NiTi thin films can be modified through melt-mediated laser processing within the partial melting regime. The extent of modification can be controlled through changes in the induced melt depth by changing the incident laser energy density. The strength of the (110) texture was shown to increase with increasing melt depth and is attributed to abnormal grain growth caused by surface energy anisotropies in BCC-structures materials. A three-dimensional Monte Carlo grain growth model was developed to aid in predicting the resulting texture for different melt depths and was shown to accurately predict texture formation within the partial melting regime. Overall texture strength was limited, however, due to the amount of grain growth achievable within a 1 $\mu$m thick film. It is considered that processing within the complete or near-complete melting regimes may allow for greater texture strength if amorphization of the film can be suppressed. The work described above shows that laser crystallization is a viable mechanism for adjusting the preferred orientation of NiTi thin films and can be used to optimize films' shape memory properties for specific applications. The Monte Carlo model developed in this work also allows for prediction of textures in partially melted NiTi films developed through surface energy induced abnormal grain growth.

## Acknowledgment

The authors would like to acknowledge Professor James S. Im of the Materials Science Program in the Department of Applied Physics and Applied Mathematics at Columbia University for allowing the use of his equipment. Financial support from Columbia University is also acknowledged.

## References

[1] Bellouard, Y., 2008, "Shape Memory Alloys for Microsystems: A Review From a Material Research Perspective," Mater. Sci. Eng., A, **481–482**, pp. 582–589.
[2] Morgan, N. B., 2004, "Medical Shape Memory Alloy Applications—The Market and Its Products," Mater. Sci. Eng. A, **378**, pp. 16–23.
[3] Ishida, A., Sato, M., Takei, A., and Miyazaki, S., 1995, "Effect of Heat Treatment on Shape Memory Behavior of Ti-rich Ti-Ni Thin Films," Mater. Trans., **36**, pp. 1349–1355. Available at http://www.jim.or.jp/journal/e/pdf3/36/11/1349.pdf
[4] Satoh, G., Birnbaum, A., and Yao, Y. L., 2010, "Annealing Effect on the Shape Memory Properties of Amorphous NiTi Thin Films," ASME J. Manuf. Sci. Eng., **132**(5), p. 051004.
[5] Birnbaum, A. J., Satoh, G., and Yao, Y. L., 2009, "Functionally Grading the Shape Memory Response in NiTi Films: Laser Irradiation," J. Appl. Phys., **106**, p. 043504.
[6] Birnbaum, A. J., Chung, U. J., Huang, X., Im, J. S., Ramirez, A. G., and Yao, Y. L., 2009, "Substrate Temperature Effects on Laser Crystallized NiTi Thin Films," J. Appl. Phys., **105**, p. 073502.
[7] Gisser, K., Busch, J., Johnson, A., and Ellis, A., 1992, "Oriented Nickel-Titanium Shape Memory Alloy Films Prepared by Annealing During Deposition," Appl. Phys. Lett., **61**, pp. 1632–1634.
[8] Popov, P., and Lagoudas, D. C., 2007, "A 3D Constitutive model for Shape Memory Alloys Incorporating Pseudoelasticity and Detwinning of Self-Accommodated Martensite," Int. J. Plast., **23**, pp. 1679–1720.
[9] Gall, K., Dunn, M., Liu, Y., Labossiere, P., Sehitoglu, H., and Chumlyakov, Y., 2002, "Micro and Macro Deformation of Single Crystal NiTi," J. Eng. Mater. Technol., **124**, pp. 238–245.
[10] Miyazaki, S., No, V., Kitamura, K., Khantachawana, A., and Hosoda, H., 2000, "Texture of Ti-Ni Rolled Thin Plates and Sputter-Deposited Thin Films," Int. J. Plast., **16**, pp. 1135–1154.
[11] Okolo, B., Welzel, U., Lamparter, P., Wagner, T., and Mittemeijer, E., 2001, "Texture of Sputtered Thin Copper Films on Amorphous $SiO_2$ and $Si_3N_4$ Substrates," Mater. Res. Soc. Symp. Proc., **695**, p. L2.9.1.
[12] Choi, J., Choi, M., Chung, U., Limanov, A., and Im, J., 2006, "The Origin and Implications of (111)-Textured Grains Obtained via Nucleation and Growth of Solids in Pulsed-Laser-Quenched Al Films on $SiO_2$," Mater. Res. Soc. Symp. Proc., **979**, p. 0979-HH11-50.

[13] Pirzada, D., Trivedi, P., Field, D., and Cheng, G., 2007, "Effect of Film Thickness and Laser Energy Density on the Microstructure of a-GaAs Films After Excimer Laser Crystallization," J. Appl. Phys., **102**, p. 013519.
[14] He, M., Ishihara, R., Metselaar, W., and Beenakker, K., 2006, "⟨100⟩-Textured Self-Assembled Square-Shaped Polycrystalline Silicon Grains by Multiple Shot Excimer Laser Crystallization," J. Appl. Phys., **100**, p. 083103.
[15] Hsieh, Y., Luo, J., and Lin, W., 2000, "Improvement of the (111) Texture and Microstructures of Cu Films by Pulsed Laser Annealing," J. Mater. Sci.: Mater. Electron., **11**, pp. 675–678.
[16] Kulovits, A., Zhong, R., Wiezorek, J. M. K., and Leonard, J. P., 2009, "Electron Microscopy of Geometrically Confined Copper Thin Films After Lateral Solidification," Thin Solid Films, **517**, pp. 3629–3634.
[17] Nash, P., and Schwarz, R. B., 1988, "Calculation of the Glass Forming Range in Binary Metallic Systems Using Thermodynamic Models," Acta Metall., **36**, pp. 3047–3053.
[18] Im, J. S., Kim, H. J., and Thompson, M. O., 1993, "Phase Transformation Mechanisms Involved in Excimer Laser Crystallization of Amorphous Silicon Films," Appl. Phys. Lett., **63**, pp. 1969–1971.
[19] Lee, H. J., and Ramirez, A. G., 2004, "Crystallization and Phase Transformations in Amorphous NiTi Thin Films for Microelectromechanical Systems," Appl. Phys. Lett., **85**, pp. 1146–1148.
[20] Smith, R. W., 1996, "A Kinetic Monte Carlo Simulation of Fiber Texture Formation During Thin-Film Deposition," J. Appl. Phys., **81**, pp. 1196–1203.
[21] Srolovitz, D., 1986, "Grain Growth Phenomena in Films: A Monte Carlo Approach," J. Vac. Sci. Technol., **4**, pp. 2925–2931.
[22] Zhang, J., Ma, F., and Xu, K., 2003, "Calculation of the Surface Energy of BCC Metals by Using the Modified Embedded-Atom Method," Surf. Interface Anal., **35**, pp. 662–666.
[23] Jung, J., Hwang, N., Park, Y., and Joo, Y., 2002, "Effect of Grain Boundary Energy on Surface-Energy Induced Abnormal Grain Growth in Columnar-Grained Film," Met. Mater. Int., **8**, pp. 1–5.
[24] Ratke, L., and Voorhees, P., 2002, *Growth and Coarsening*, Springer-Verlag, Berlin, pp. 67–70, Chap. IV.
[25] Raabe, D., 2000, "Scaling Monte Carlo Kinetics of the Potts Model Using Rate Theory," Acta Mater., **48**, pp. 1617–1628.
[26] Wang, X., Rein, M., and Vlassak, J. J., 2008, "Crystallization Kinetics of Amorphous Equiatomic NiTi Thin Films: Effect of Film Thickness," J. Appl. Phys., **103**, p. 023501.
[27] Clyne, T. W., 1984, "Numerical Treatment of Rapid Solidification," Metall. Trans. B, **15**, pp. 369–381.
[28] Murray, J. L., 1991, "Ni-Ti (Nickel-Titanium)," *Phase Diagrams of Binary Nickel Alloys*, P. Nash, ed., ASM International, Materials Park, OH, pp. 342–355.
[29] Kim, K. S., Jee, K. K., Kim, W. C., Jang, W. Y., and Han, S. H., 2008, "Effect of Heat Treatment Temperature on Oxidation Behavior in Ni-Ti Alloy," Mater. Sci. Eng., A, **481–482**, pp. 658–661.
[30] Thompson, C., and Carel, R., 1996, "Stress and Grain Growth in Thin Films," J. Mech. Phys. Solids, **5**, pp. 657–673.